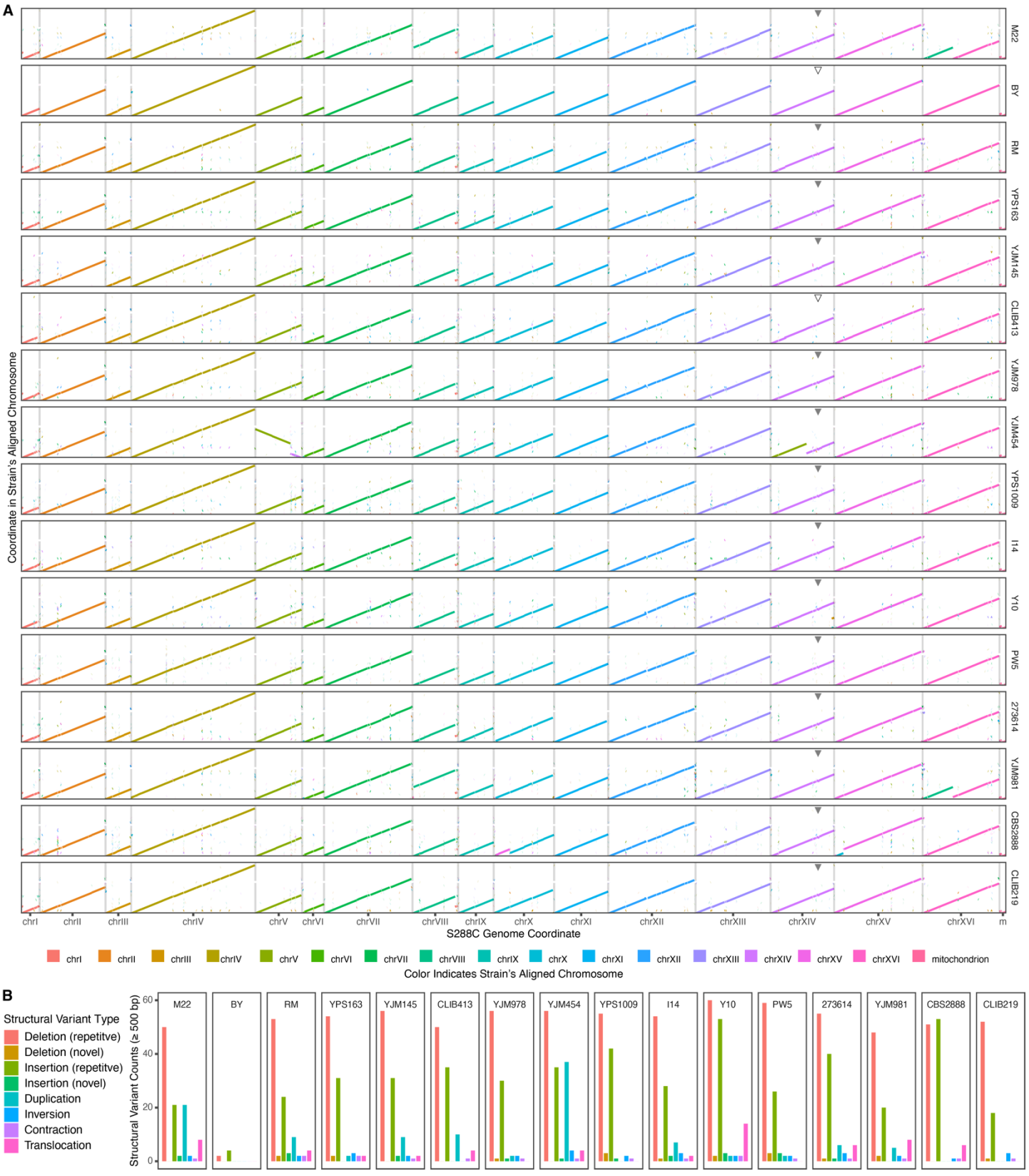

Figure S1. Structural variation in the 16 assembled genomes.
A. Alignment of the 16 genome assemblies to the S288C reference genome. Arrowheads indicate the position of a recurrent inversion on Chr XIV, with unfilled and filled arrowheads for strains with the reference and inverted orientation, respectively. Translocations are seen in strains M22, YJM454, YJM981, and CBS2888. **B.** Counts of classes of structural variants larger than 500 bp in the 16 genome assemblies. Most of the duplications in strain YJM454 correspond to an expansion of the YGR201C locus, illustrated in Supplemental Fig. 3.

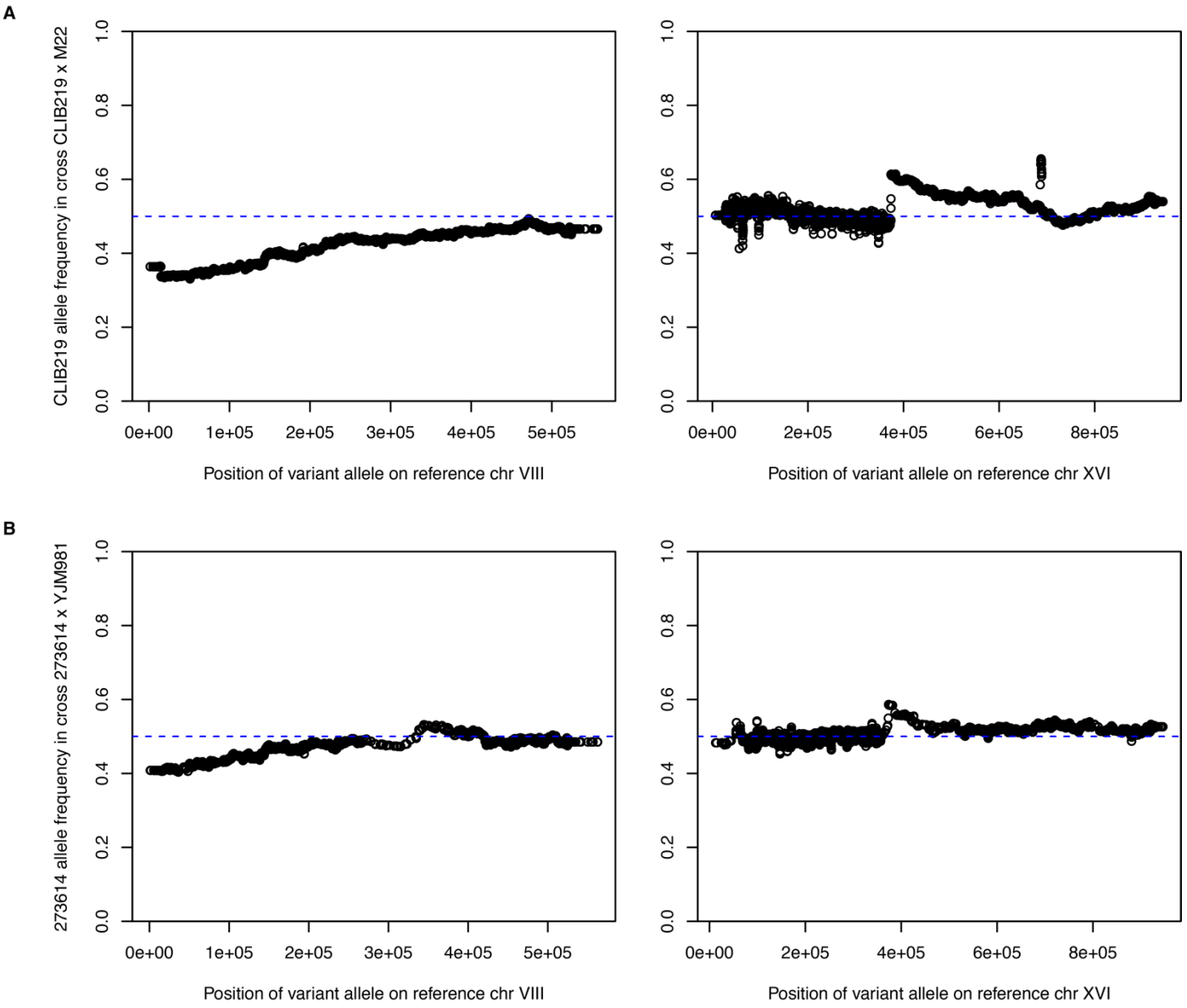

Figure S2. Allele frequency skews in strains M22 and YJM981 caused by a translocation between the left arms of Chr VIII and XVI.

A. Strain CLIB219 allele frequencies on Chr VIII (left) and Chr XVI (right) in segregants of the CLIB219 × M22 cross. **B.** Strain 273614 allele frequencies on Chr VIII (left) and Chr XVI (right) in segregants of the 273614 × YJM981 cross. As described by Hou et al., there are essential genes present on the translocated fragment of Chr XVI but not Chr VIII, so inheritance of the VIII-XVI fusion along with the untranslocated VIII is lethal, while all other combinations are viable. This is consistent with the observed depletion of markers on the left of Chr VIII associated with the parent lacking the translocation and depletion of markers to the right of position 370,000 of Chr XVI associated with the parent carrying the translocation.

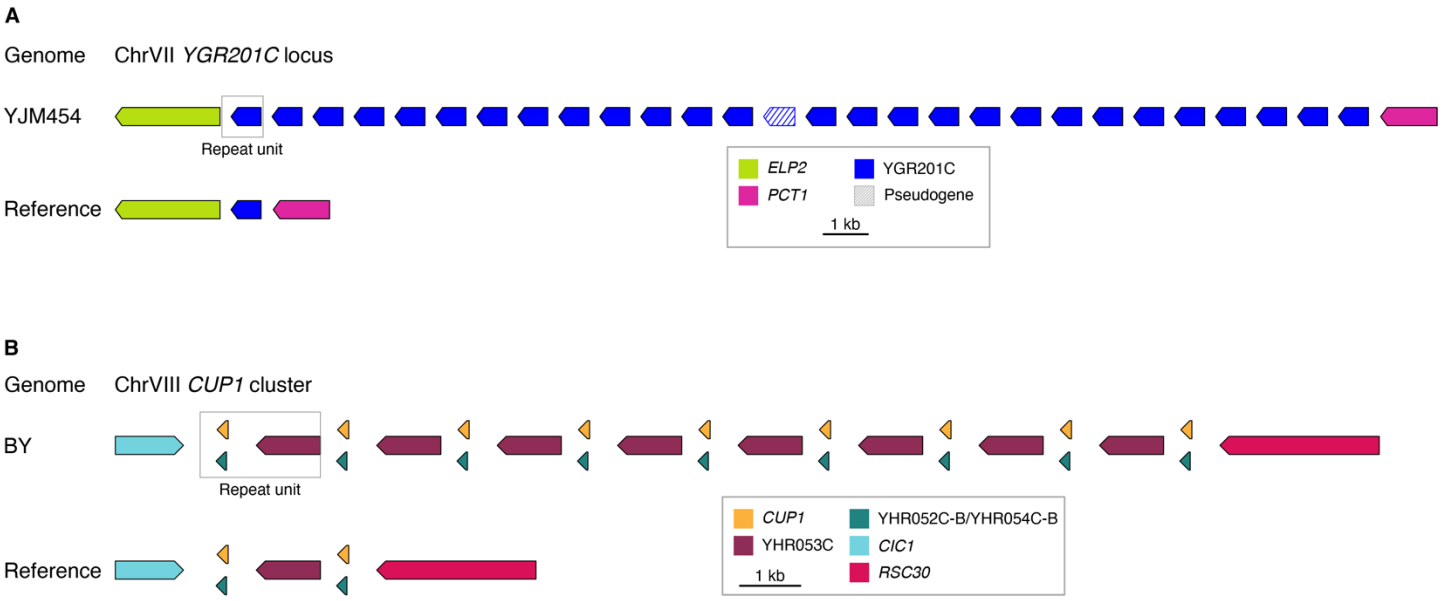

Figure S3. Repetitive loci in the sequenced genomes
A. Comparison of the YGR201C tandem repeats in strain YJM454 and the S288C reference genome. **B.** Diagrams of the genes in the *CUP1* loci of the BY assembled genome and S288C reference genome. The reference genome was assembled from Sanger sequencing reads, which will not span the length of a *CUP1* repeat unit (1998 bp). The expanded *CUP1* array includes seven additional copies each of *CUP1*, YHR052C-B, and YHR053C, for 21 total extra gene copies in BY relative to the reference genome.

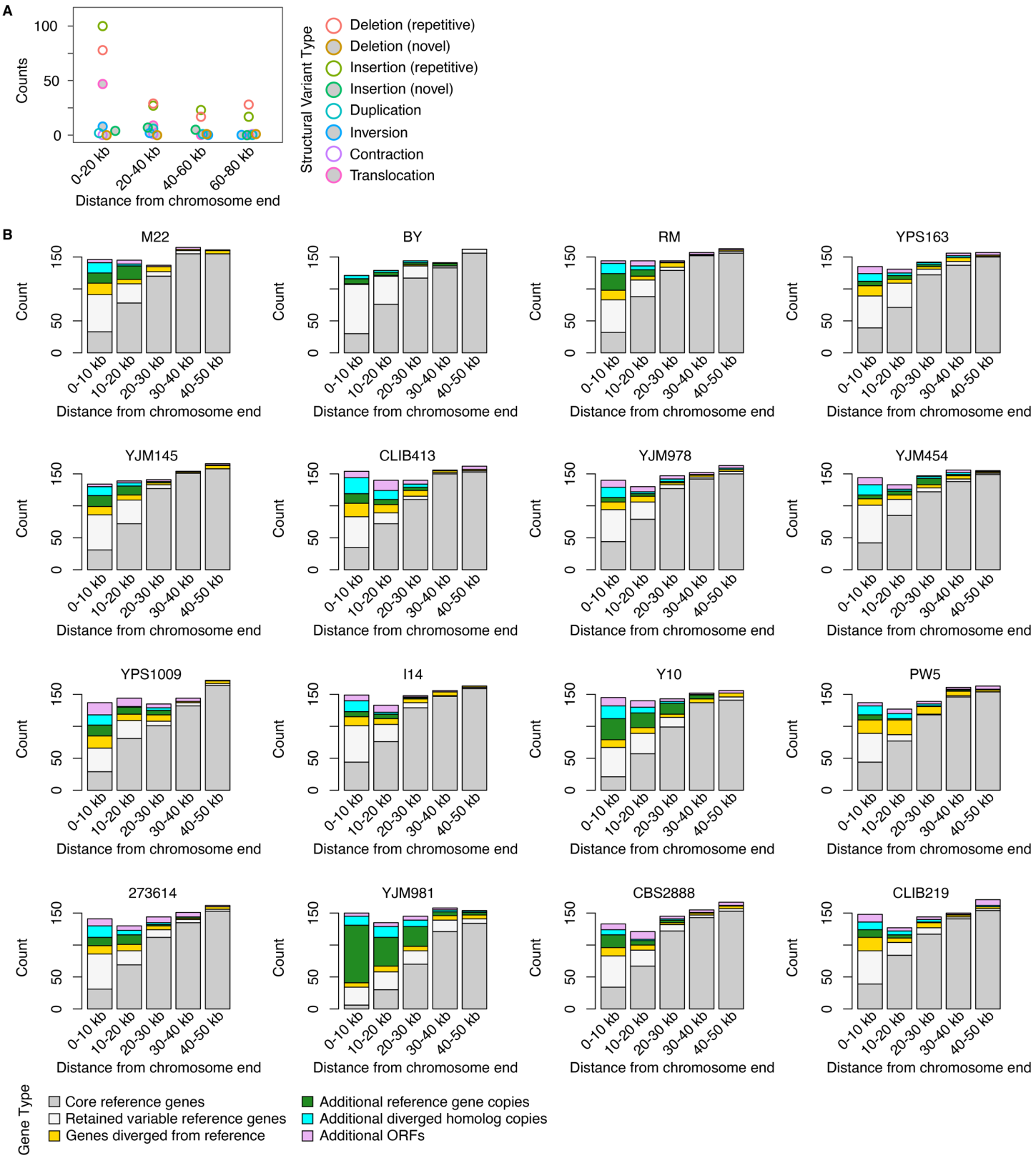

Figure S4. Structural variants and variable pangenomic genes are enriched in subtelomeric regions. **A.** Counts of different categories of structural variants in 20-kb windows of distance from the telomere for all 16 genomes combined. **B.** Counts of different categories of genes in 10-kb windows of distance from the telomere for each sequenced genome. The midpoint of a gene's start and stop coordinate was used as its position. Core reference genes were defined as those present in all 16 sequenced genomes, while variable reference genes are present in the reference genome but absent from at least one of the 16 sequenced genomes. Other categories of genes are defined as in Fig. 1C.

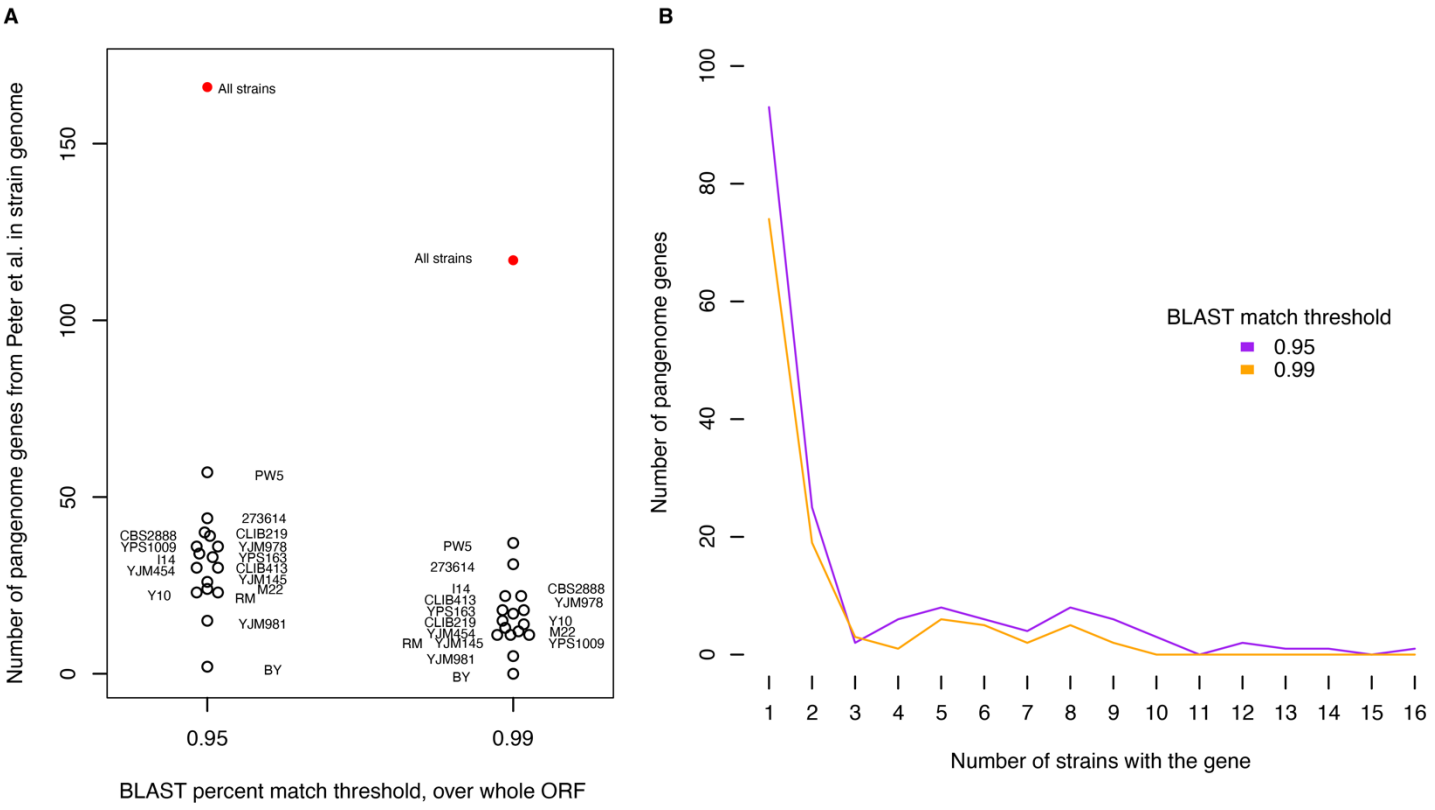

Figure S5. Representation of non-reference pangenome genes in the 16 genomes.
A. Counts of non-reference pangenome genes in each of the 16 genomes. Genes were found by BLAST searches of pangenome gene sequences against the gene sequences from each genome. The percent match over the whole ORF was determined by multiplying the percent match over the length of the BLAST alignment by the ratio of the length of the aligned sequence to the length of the non-reference pangenome ORF. The analysis was conducted using 1337 non-reference pangenome genes that started with an ATG, encoded over 100 amino acids, and had no ambiguous bases, out of 1767 total non-reference pangenome genes annotated by Peter et al. **B.** Frequency of represented non-reference pangenome genes across the 16 genomes. Most were found in a single strain.

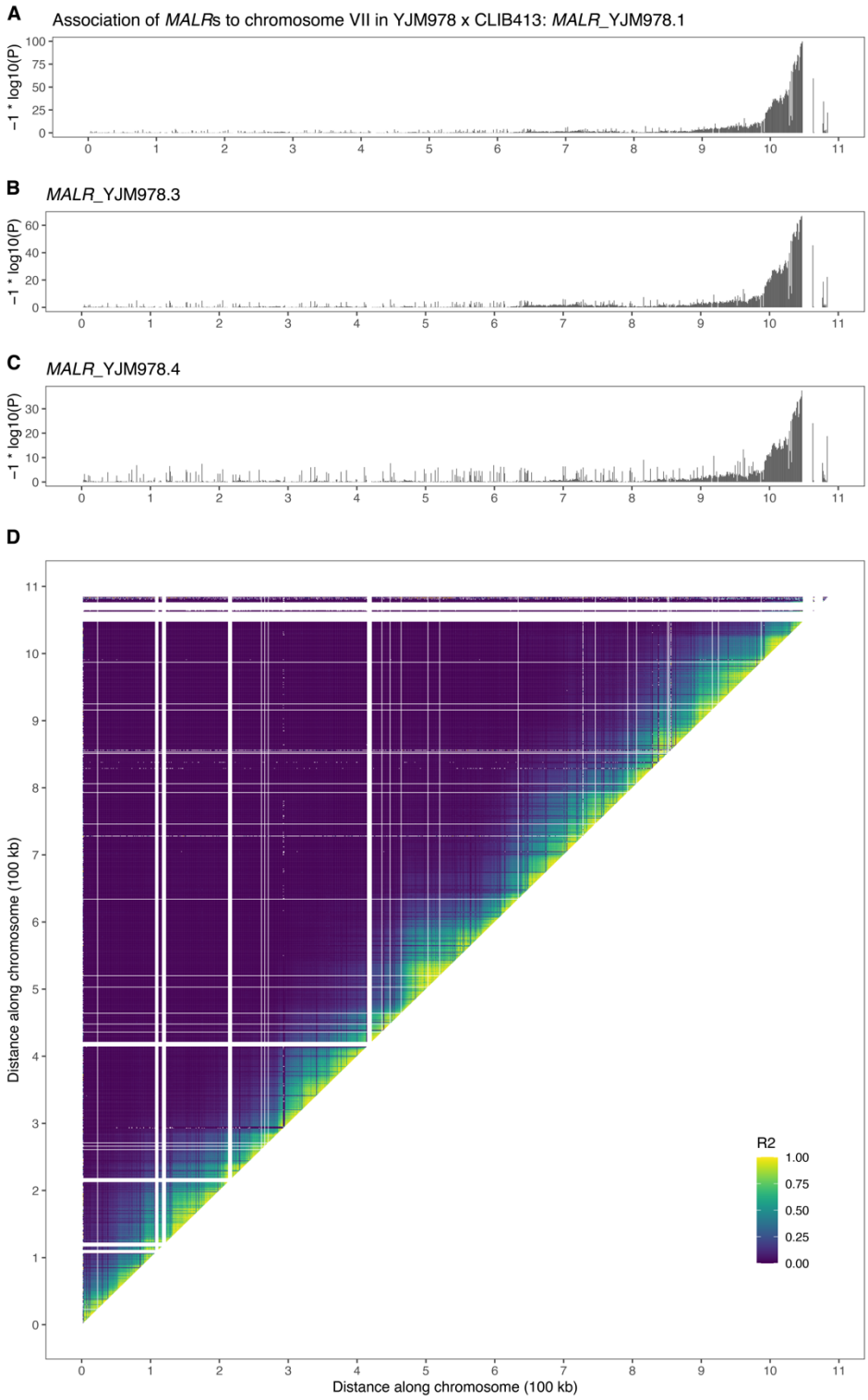

Figure S6. Validation of assembly of YJM978 *MALR*s onto Chr VII-R through linkage mapping in YJM978 × CLIB413.

A-C. Chr VII linkage mapping of $MALR_{YJM978.1}$, $MALR_{YJM978.3}$, and $MALR_{YJM978.4}$, representing *MAL13*, *MAL64*, and *MAL63*, respectively. For each segregant in the YJM978 × CLIB413 cross, the presence of Illumina short reads matching the query gene sequence was determined using bwa, and quantified as reads per million. This value was treated as a quantitative trait and mapped in the YJM978 × CLIB413 segregant panel using SNPs on Chr VII segregating between YJM978 and CLIB413. Association values are plotted against Chr VII coordinates. Note that $MALR_{YJM978.2}$ (representing *MAL83*) was not tested, as *MAL83* is present on the right arm of both the YJM978 and CLIB413 Chr VII assemblies and thus is predicted to be inherited in 100% of segregants, which blocks the use of linkage to confirm its chromosomal location.

D. Linkage disequilibrium plot of segregating genotypes on Chr VII in YJM978 × CLIB413. There is high correlation along the entire diagonal with no completely disjoint linkage blocks. This indicates that the Chr VII assemblies in YJM978 and CLIB413 did not incorrectly concatenate a different chromosome's sequence onto the end of Chr VII, which could lead to misannotation of *MALR*s onto Chr VII. White segments denote missing data due to the lack of suitable SNPs for genotyping segregants in that window.

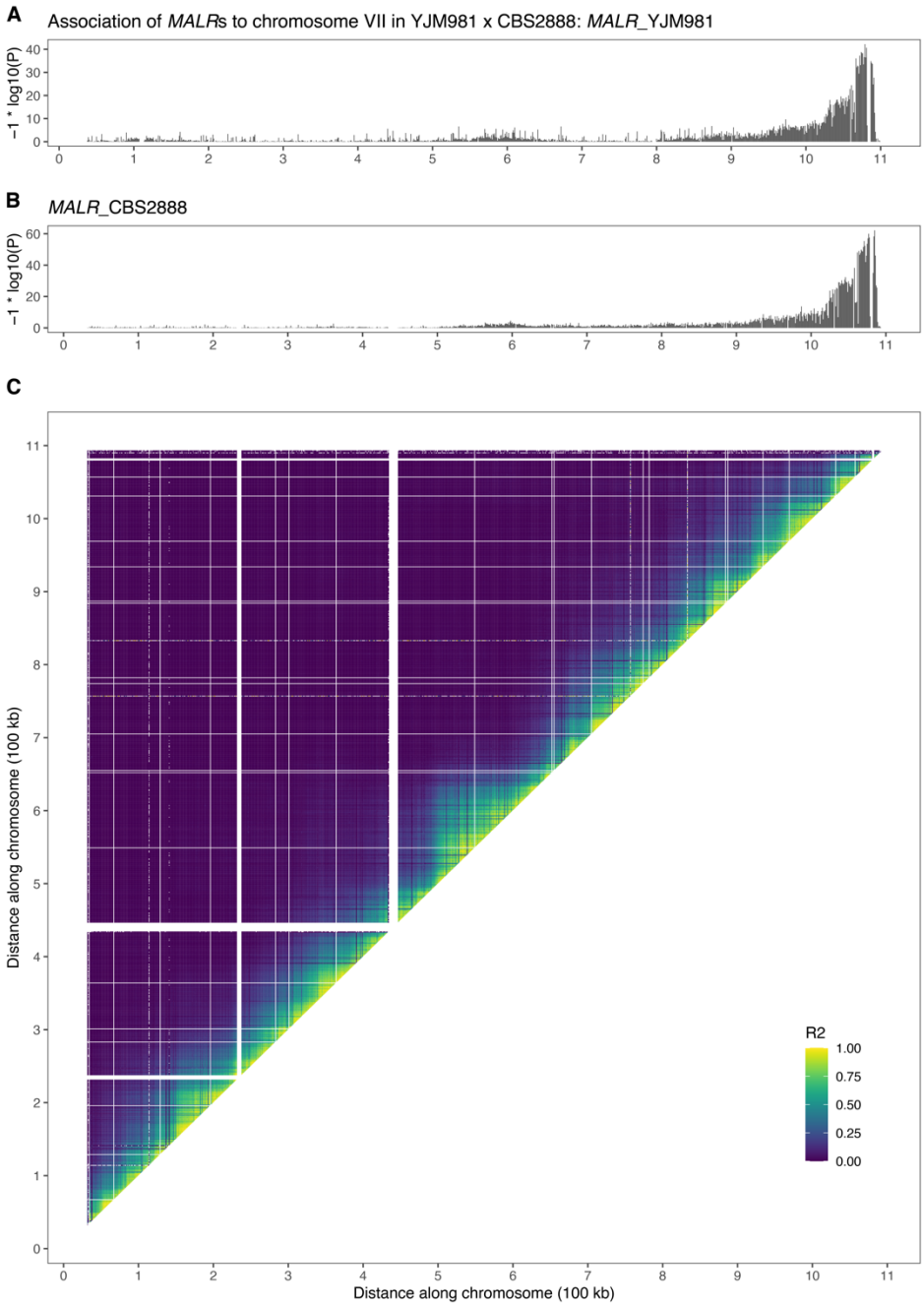

Figure S7. Validation of assembly of *MALR*$_{YJM981}$ and *MALR*$_{CBS2888}$ onto Chr VII-R through linkage mapping in YJM981 × CBS2888.

A-B. Chr VII linkage mapping of *MALR*$_{YJM981}$ and *MALR*$_{CBS2888}$, representing *MAL23* and *MAL83*, respectively. Association is shown as in Supplemental Fig. 6A-C.

C. Linkage disequilibrium plot of segregating genotypes on Chr VII in YJM981 × CBS2888. Linkage disequilibrium is shown as in Supplemental Fig. 6D.

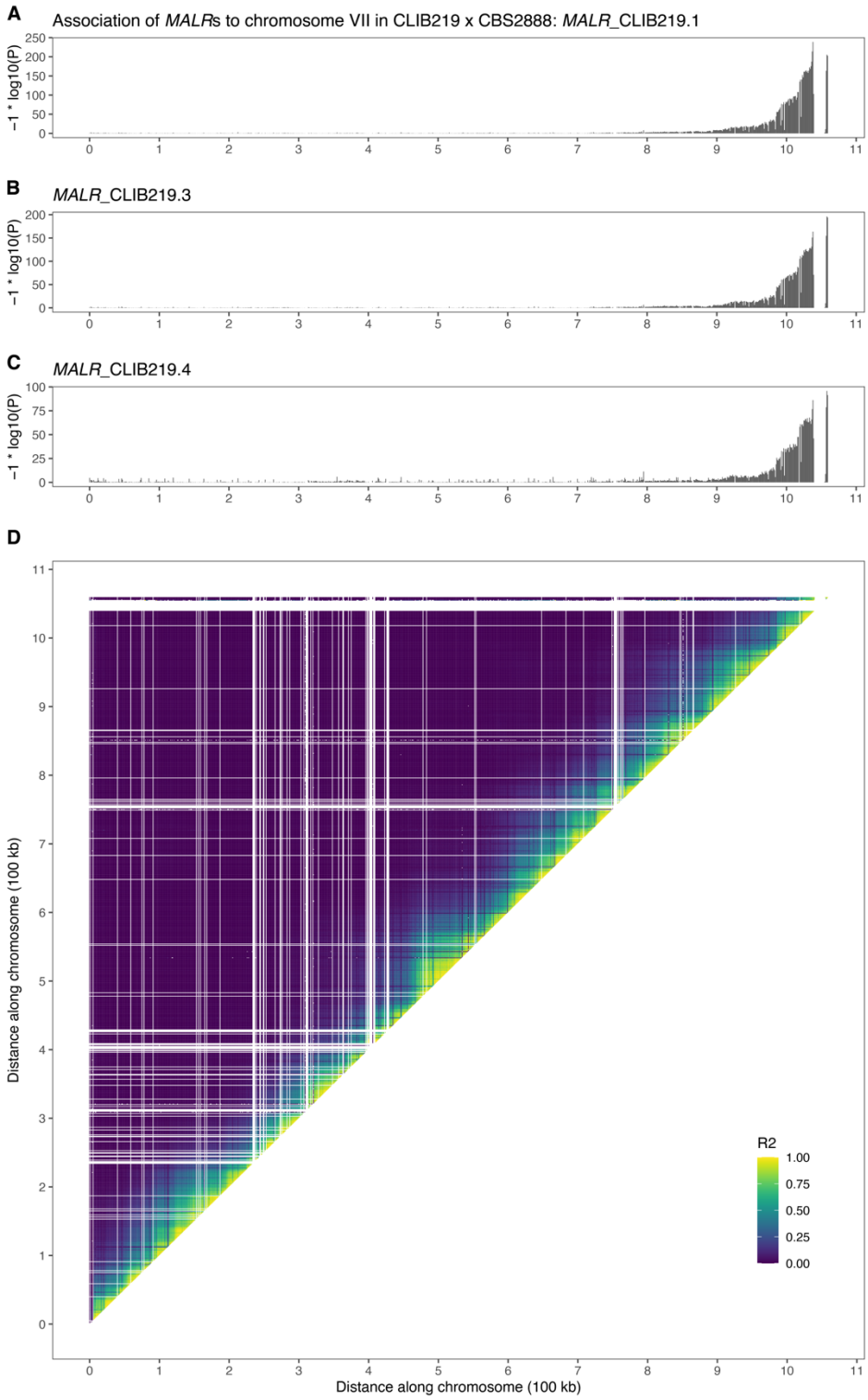

Figure S8. Validation of assembly of CLIB219 *MALR*s onto Chr VII-R through linkage mapping in CLIB219 × CBS2888.

A-C. Chr VII linkage mapping of $MALR_{CLIB219.1}$, $MALR_{CLIB219.3}$, and $MALR_{CLIB219.4}$, representing *MAL13*, *MAL64*, and *MAL43*, respectively. Association is shown as in Supplemental Fig. 6A-C. As in Supplemental Fig. 6, $MALR_{CLIB219.2}$ (representing *MAL83*) was not tested, as *MAL83* is present on the right arm of both the CLIB219 and CBS2888 Chr VII assemblies.

D. Linkage disequilibrium plot of segregating genotypes on Chr VII in CLIB219 × CBS2888. Linkage disequilibrium is shown as in Supplemental Fig. 6D.

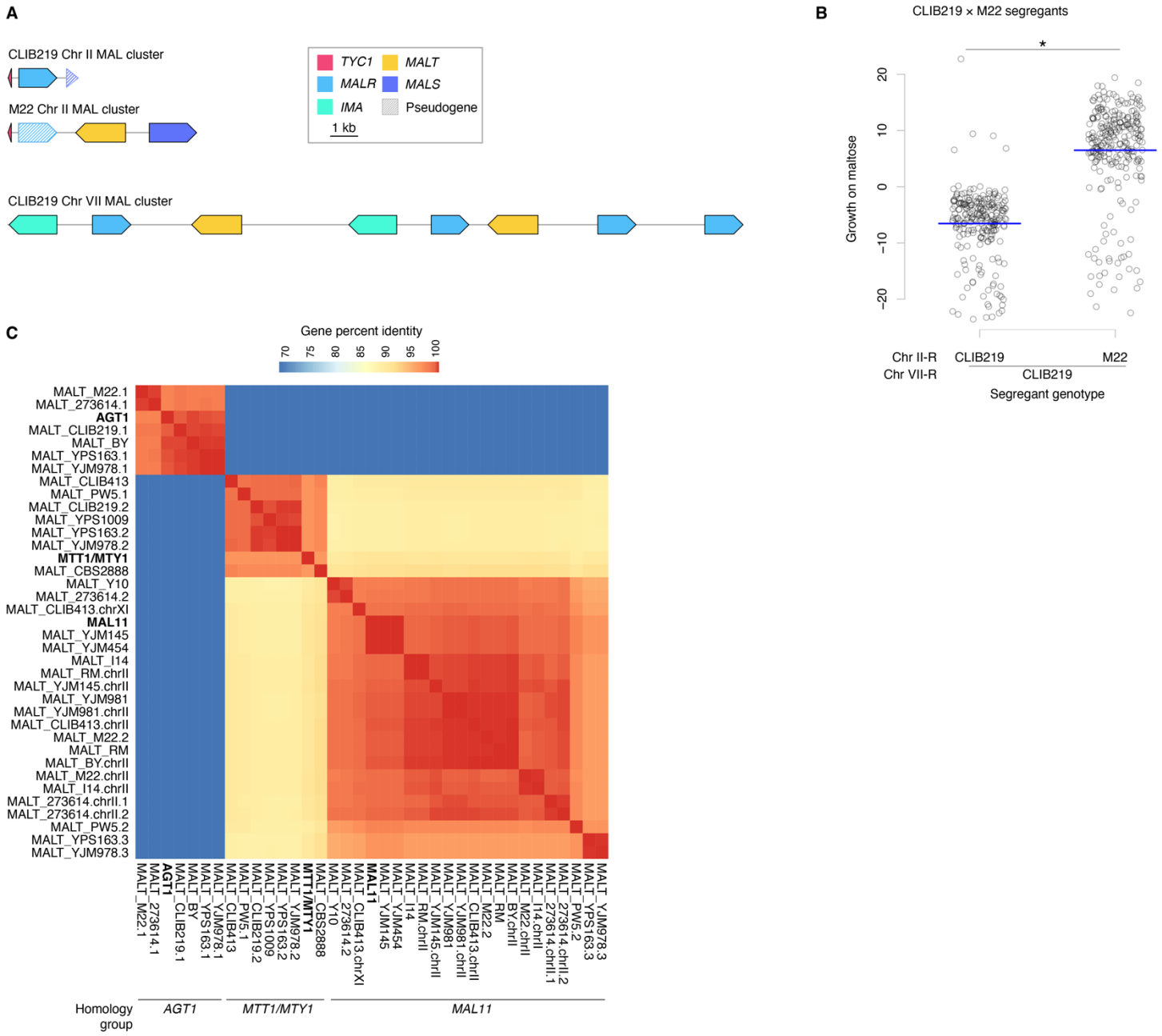

Figure S9. Variation in *MALS* and *MALT*.
A. Diagram of *MAL* genes found in strains CLIB219 and M22 at the right end of Chr II. The *MAL* genes found in strain CLIB219 on Chr VII are also shown for reference. **B.** Scatterplot of maltose growth of segregants with the CLIB219 Chr VII *MAL* cluster in the CLIB219 x M22 cross, with segregants partitioned by Chr II *MAL* cluster genotype. Plots are shown as in Fig. 3, with normalization to glucose growth. Mean phenotypes are demarcated with blue lines. (* p < 5e-64, two-tailed Student's *t*-test.) **C.** DNA percent identity between *MALT* genes in the 16 strains. Percent ID was determined using Clustal Omega (McWilliam et al. 2013). We included all *MALT* genes found anywhere in the 16 strains; note that MALT_M22.1 and MALT_273614.1 are annotated as pseudogenes in Fig. 2 due to a nonsense mutation 26 codons from the end, as in Gallone et al. Genes are labeled with a chromosome identifier, except for those found on Chr VII. Previously characterized *MALT* genes are included for reference, with names in bold. Sequences of previously characterized *MALT* genes were obtained from NCBI refseq, with accession IDs L47346 for *AGT1*, AJ491328 for *MTT1/MTY1*, and AJ012752 for *MAL11*. Note that these gene names are not the same as those on the yeast genome database, where the gene *MAL11* (here named MALT_BY) is closest to the published *AGT1*, whereas the gene *MAL31* (here named MALT_BY.chrII) is closest to the published *MAL11. MALT*s with greater than 97% sequence identity are sorted into homology groups, labeled at the bottom.

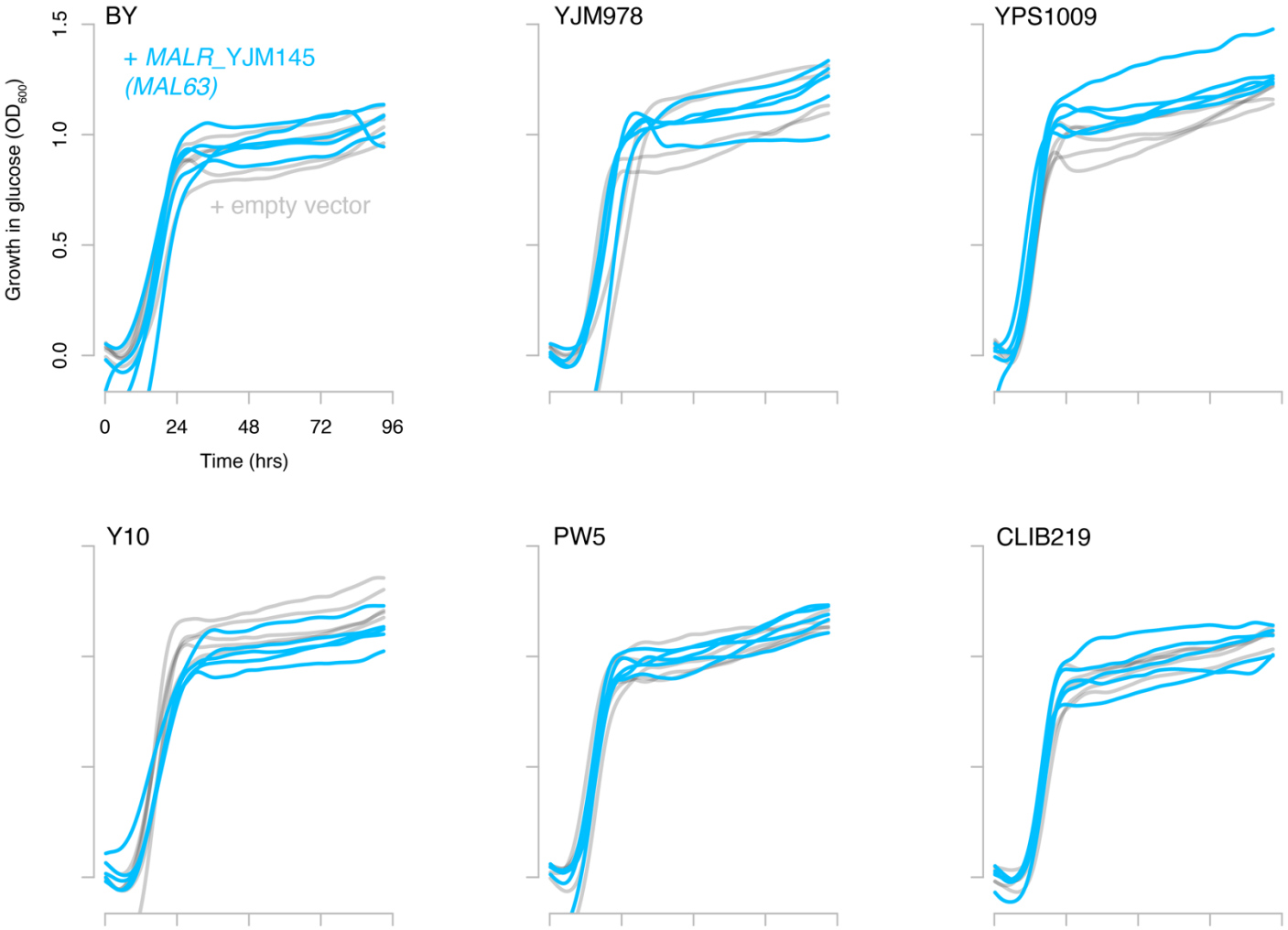

Figure S10. Growth in glucose is unaffected by *MALR* content.
Growth over time in glucose for strains BY, YJM978, YPS1009, Y10, PW5, and CLIB219 transformed with a plasmid expressing $MALR_{YJM145}$ (blue) or empty vector (grey). n = 5 biological replicates, except for YJM978 + empty vector, which had 4 biological replicates. Background absorbance was subtracted, calculated from the ODs of the strains grown without sugar.

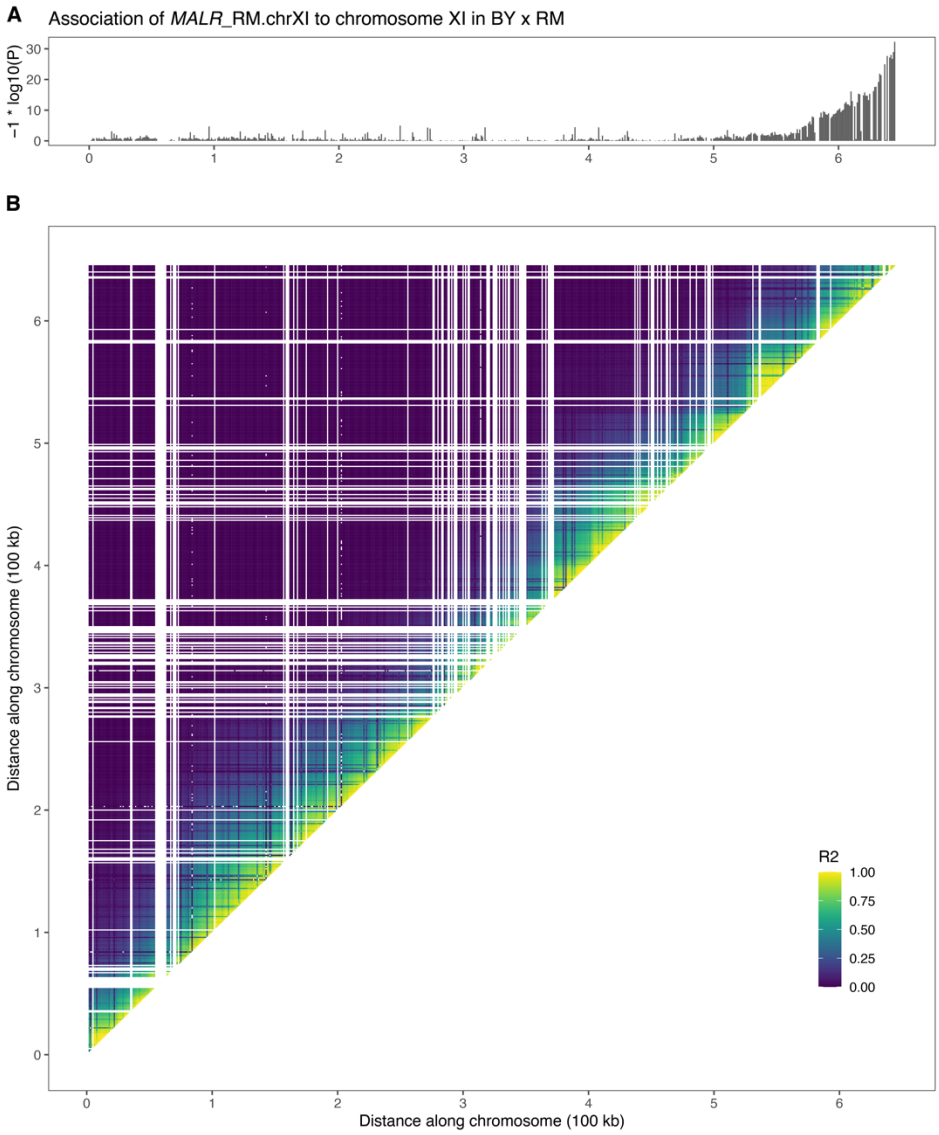

Figure S11. Validation of assembly of *MALR*$_{\text{RM.chrXI}}$ onto Chr XI-R through linkage mapping in BY × RM.
A. Chr XI linkage mapping of *MALR*$_{\text{RM.chrXI}}$. Association is shown as in Supplemental Fig. 6A-C.
B. Linkage disequilibrium plot of segregating genotypes on Chr XI in BY × RM. Linkage disequilibrium is shown as in Supplemental Fig. 6D.

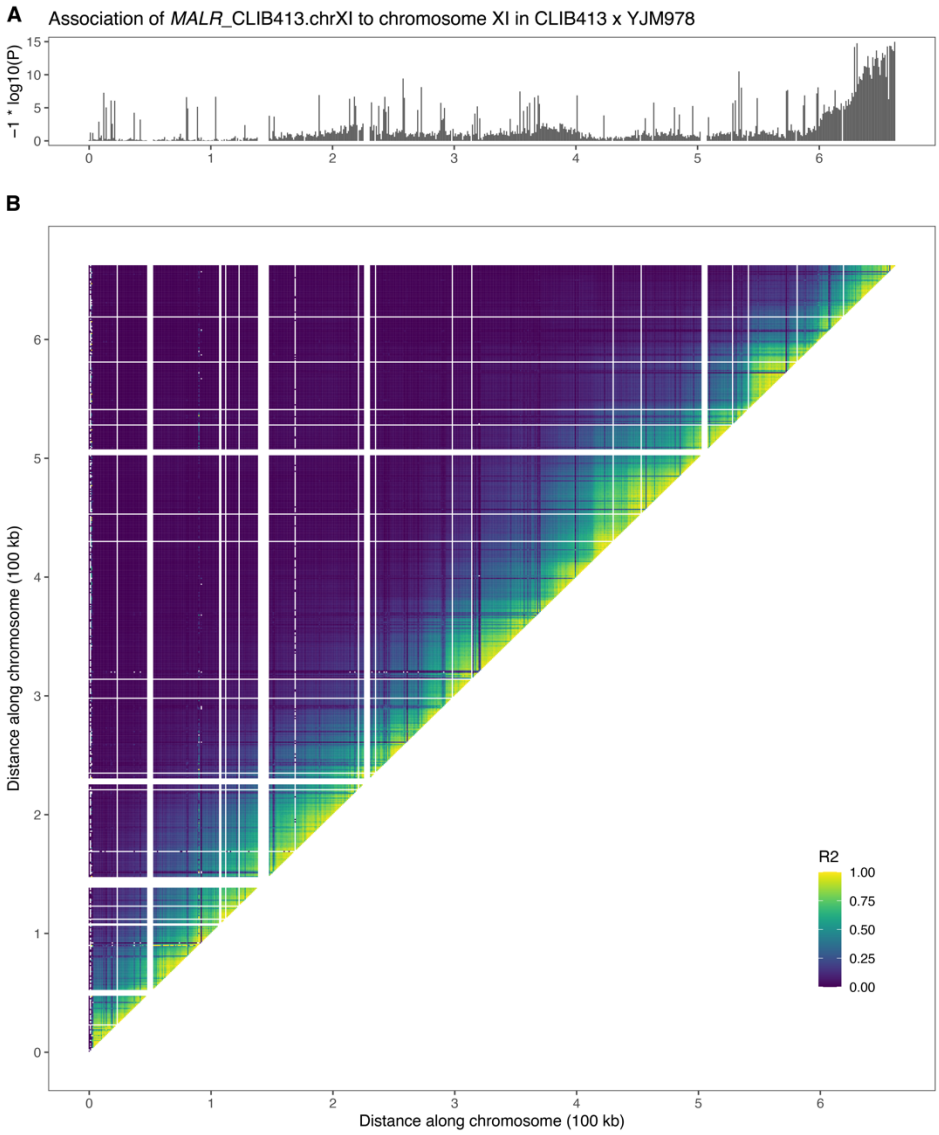

Figure S12. Validation of assembly of *MALR*$_{\text{CLIB413.chrXI}}$ onto Chr XI-R through linkage mapping in CLIB413 × YJM978.

A. Chr XI linkage mapping of *MALR*$_{\text{CLIB413.chrXI}}$. Association is shown as in Supplemental Fig. 6A-C.

B. Linkage disequilibrium plot of segregating genotypes on Chr XI in CLIB413 × YJM978. Linkage disequilibrium is shown as in Supplemental Fig. 6D.

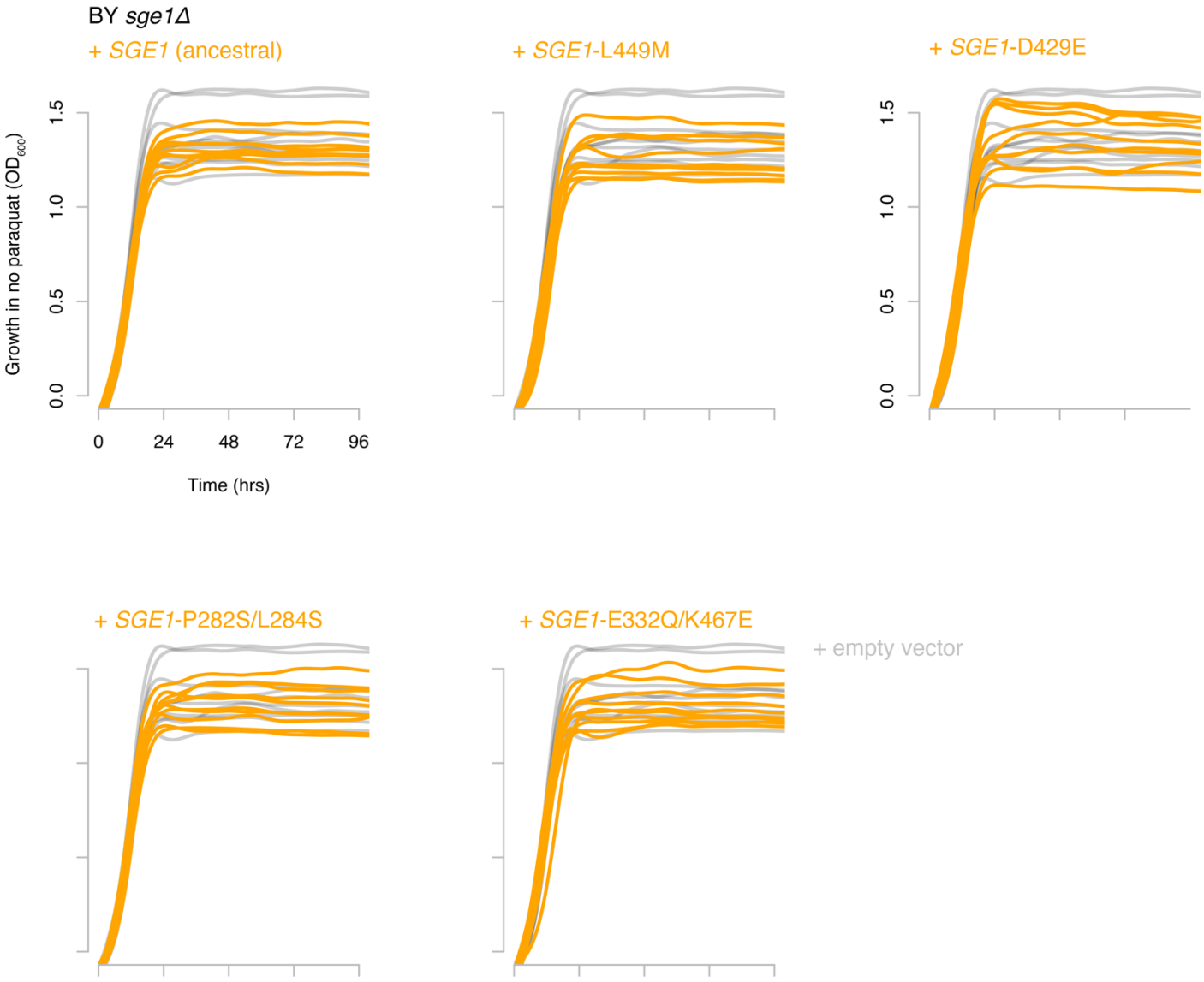

Figure S13. Expression of *SGE1* alleles does not affect growth in media without paraquat. Growth over time in liquid YPD media for BY *sge1Δ* transformed with plasmids expressing *SGE1* alleles from strains BY, YJM145, YPS1009, I14, or 273614 (orange). Growth curves are overlaid onto growth curves of *sge1Δ* transformed with empty vector (grey) for comparison. *n* = 10 biological replicates. Background absorbance at *t* = 0 was subtracted from all other timepoints for each curve.

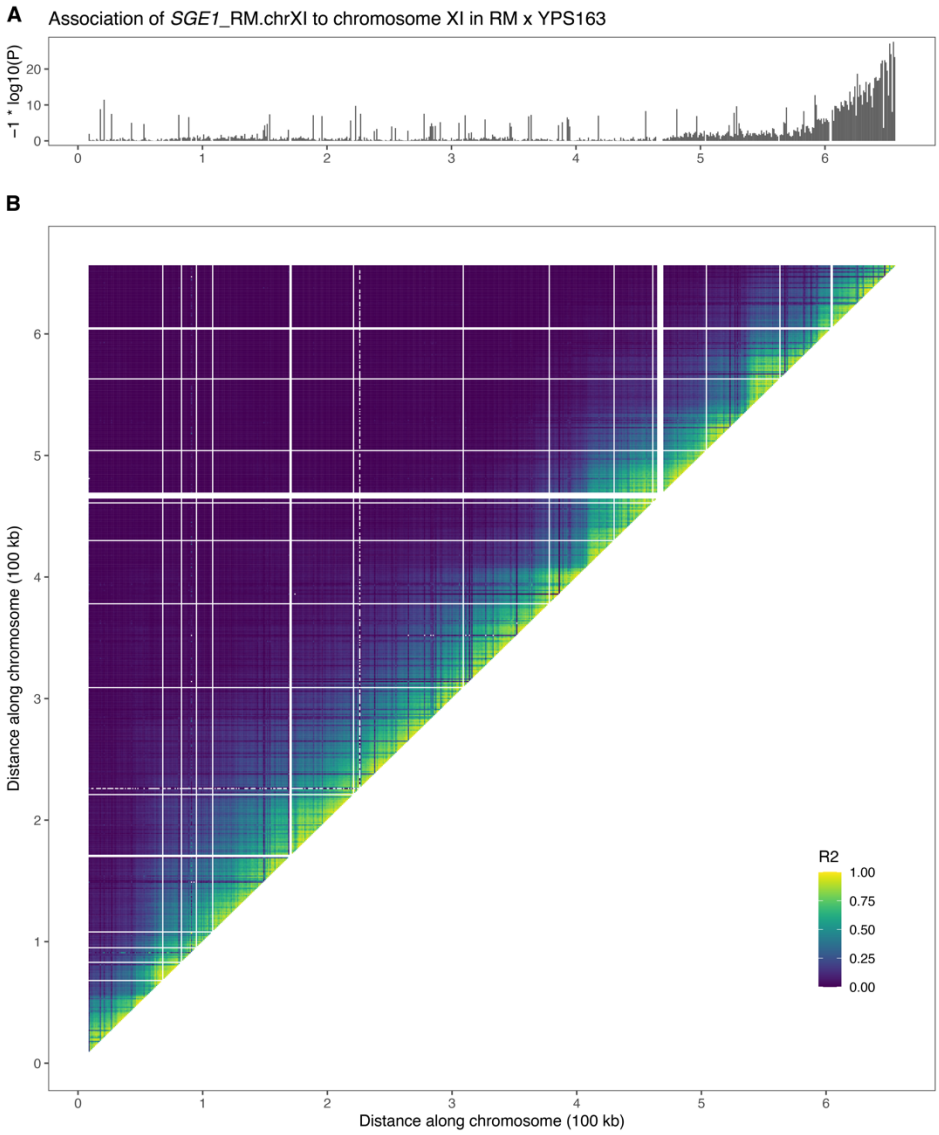

Figure S14. Validation of assembly of *SGE1*$_{\text{RM.chrXI}}$ onto Chr XI-R through linkage mapping in RM × YPS163.
A. Chr XI linkage mapping of *SGE1*$_{\text{RM.chrXI}}$. Association is shown as in Supplemental Fig. 6A-C.
B. Linkage disequilibrium plot of segregating genotypes on Chr XI in RM × YPS163. Linkage disequilibrium is shown as in Supplemental Fig. 6D.

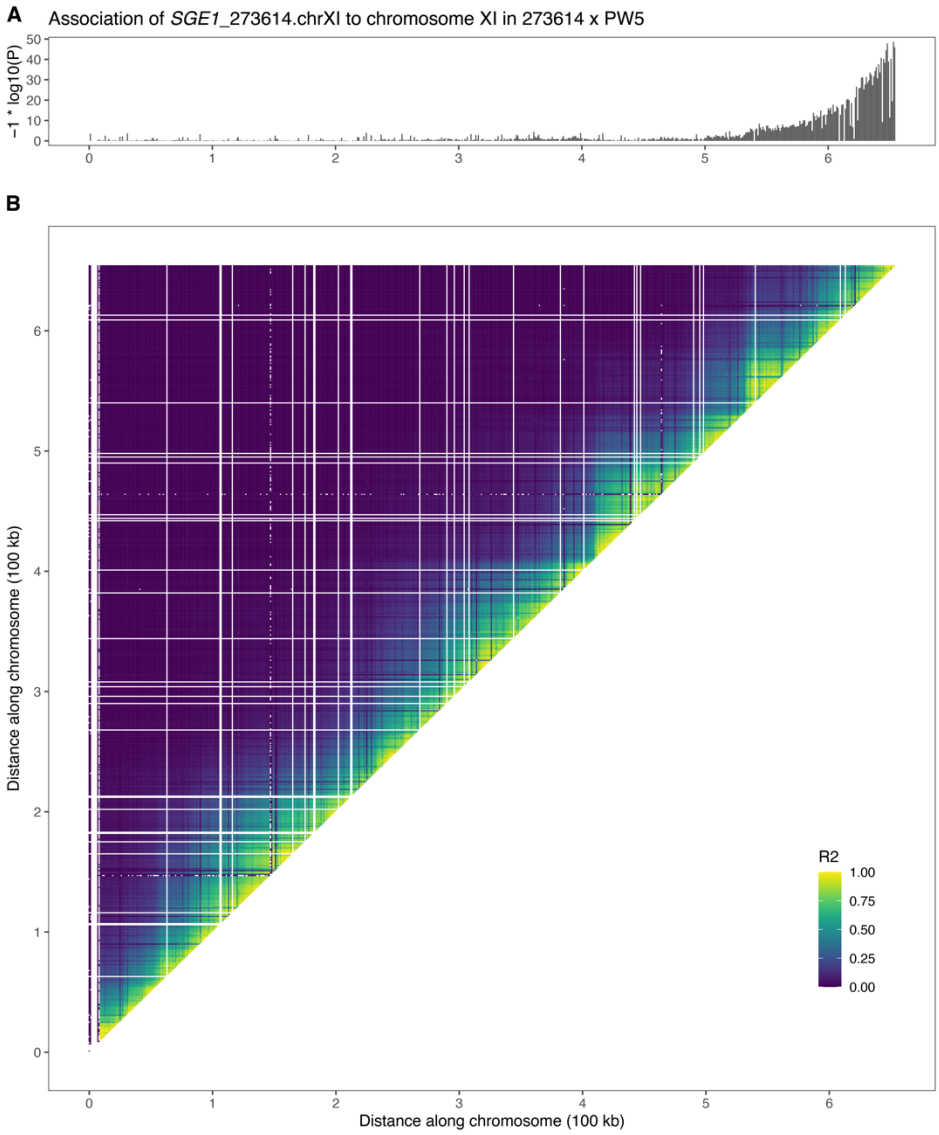

Figure S15. Validation of assembly of *SGE1*$_{273614.chrXI}$ onto Chr XI-R through linkage mapping in 273614 × PW5.

A. Chr XI linkage mapping of *SGE1*$_{273614.chrXI}$. Association is shown as in Supplemental Fig. 6A-C.

B. Linkage disequilibrium plot of segregating genotypes on Chr XI in 273614 × PW5. Linkage disequilibrium is shown as in Supplemental Fig. 6D.

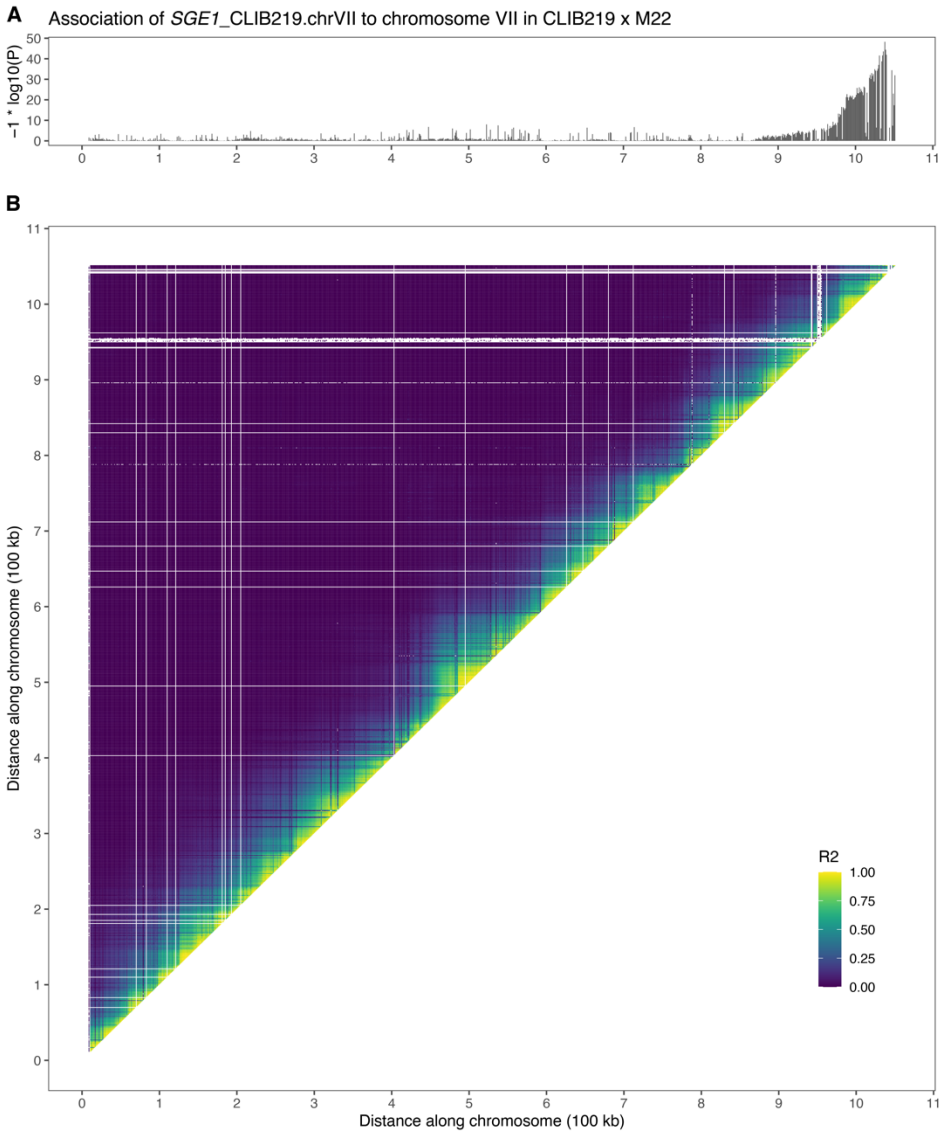

Figure S16. Validation of assembly of *SGE1*$_{\text{CLIB219.chrVII}}$ onto Chr VII-R through linkage mapping in CLIB219 × M22.

A. Chr VII linkage mapping of *SGE1*$_{\text{CLIB219.chrVII}}$. Association is shown as in Supplemental Fig. 6A-C.

B. Linkage disequilibrium plot of segregating genotypes on Chr VII in CLIB219 × M22. Linkage disequilibrium is shown as in Supplemental Fig. 6D.

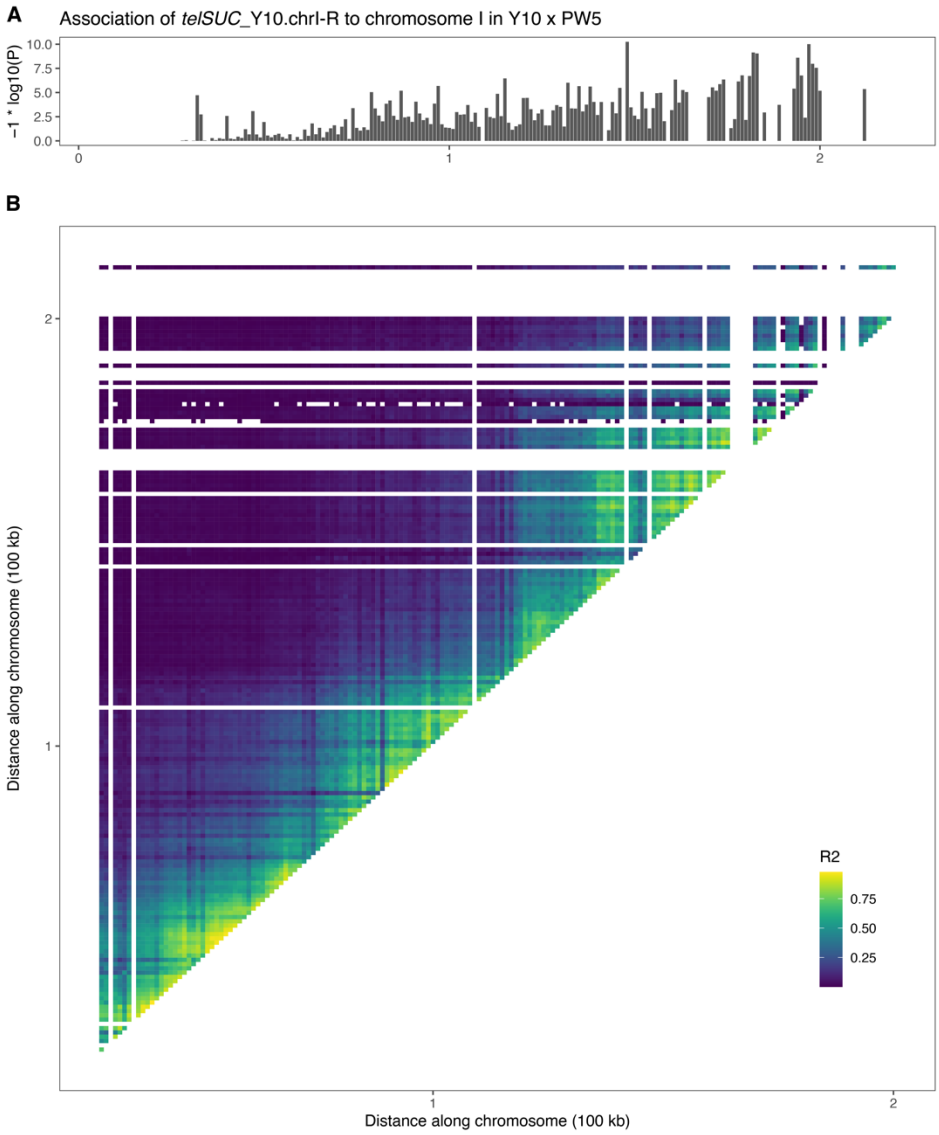

Figure S17. Validation of assembly of *telSUC*$_{\text{Y10.chrI-R}}$ onto Chr I-R through linkage mapping in Y10 × PW5.

A. Chr I linkage mapping of *telSUC*$_{\text{Y10.chrI-R}}$. Association is shown as in Supplemental Fig. 6A-C. The linkage is highly significant, but the strength of linkage is lower here than for other analyses due to the presence of identical and near-identical *telSUC* sequences at other Y10 chromosome ends. The linkage signal is also spread over a larger component of the chromosome here than for other analyses due to Chr I being very short and thus experiencing fewer recombination events.

B. Linkage disequilibrium plot of segregating genotypes on Chr I in Y10 × PW5. Linkage disequilibrium is shown as in Supplemental Fig. 6D.

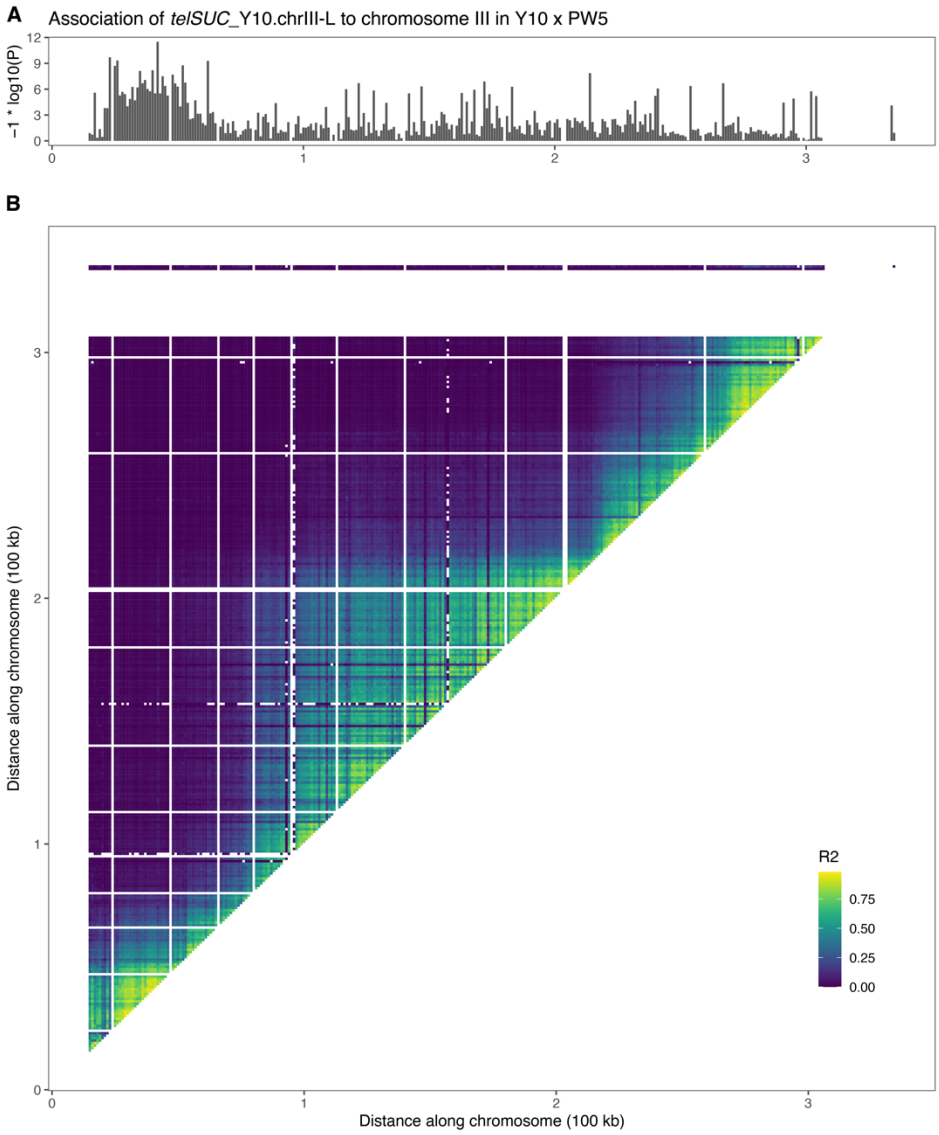

Figure S18. Validation of assembly of *telSUC*$_{\text{Y10.chrIII-L}}$ onto Chr III-L through linkage mapping in Y10 × PW5.

A. Chr III linkage mapping of *telSUC*$_{\text{Y10.chrIII-L}}$. Association is shown as in Supplemental Fig. 6A-C.

B. Linkage disequilibrium plot of segregating genotypes on Chr III in Y10 × PW5. Linkage disequilibrium is shown as in Supplemental Fig. 6D.

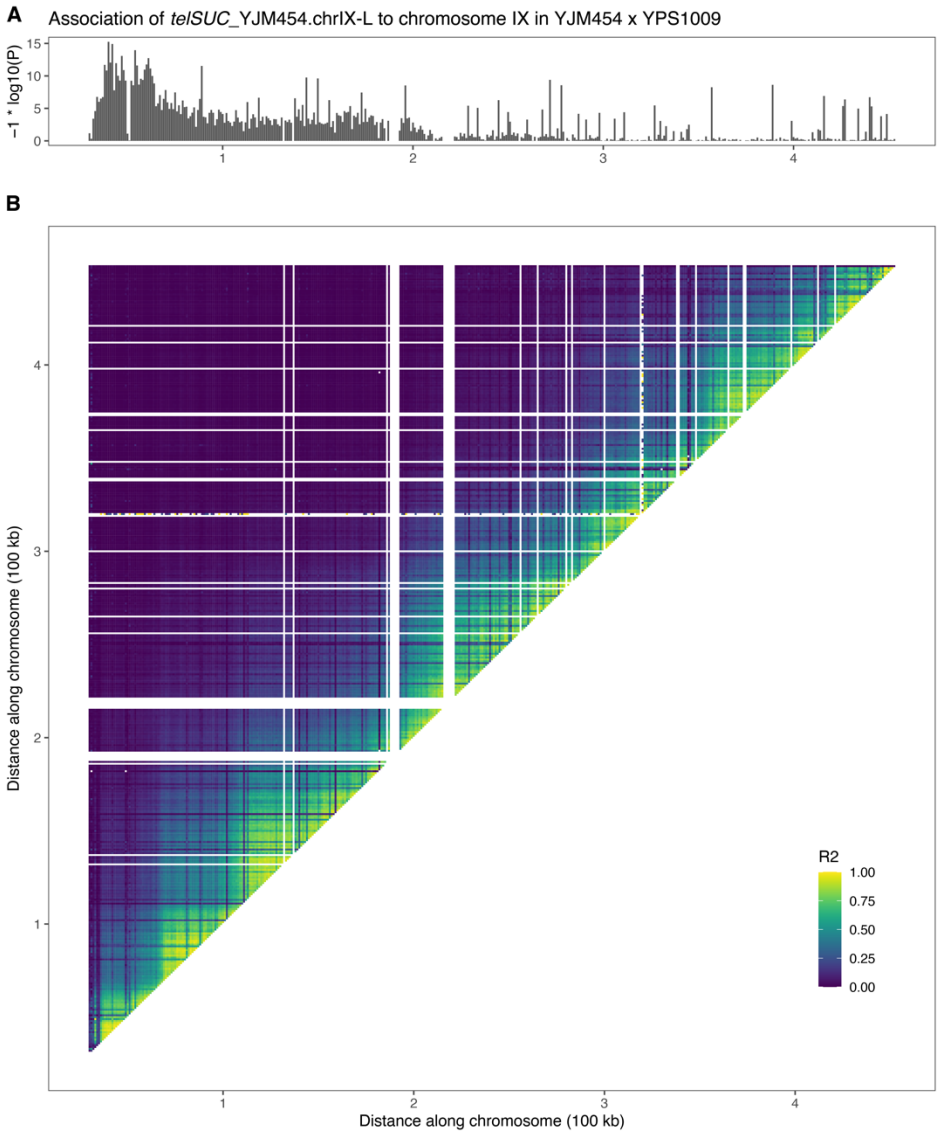

Figure S19. Validation of assembly of *telSUC*$_{\text{YJM454.chrIX-L}}$ onto Chr IX-L through linkage mapping in YJM454 × YPS1009.
A. Chr IX linkage mapping of *telSUC*$_{\text{YJM454.chrIX-L}}$. Association is shown as in Supplemental Fig. 6A-C.
B. Linkage disequilibrium plot of segregating genotypes on Chr IX in YJM454 × YPS1009. Linkage disequilibrium is shown as in Supplemental Fig. 6D.

Table S1. Assembly statistics.
Characteristics are given for the 16 genome assemblies, including the average length and number of HiFi reads and contigs, as well as Genbank accession numbers. (Included as a sheet in the Supplemental_tables.xls file.)

Table S2. Indels present in large-effect QTLs.
For QTLs mapped by Bloom et al. with LOD score greater than 75, we identified insertions or deletions relative to the reference genome larger than 250 bp that were contained within the QTL confidence interval. Note that the recurrent QTL for neomycin resistance mapping to the HO locus was caused by the use of KanMX to knock out the HO gene in a subset of strains, rather than by natural variation. (Included as a sheet in the Supplemental_tables.xls file.)

Table S3. Strains used in the study.
(Included as a sheet in the Supplemental_tables.xls file.)

Table S4. Plasmids used in the study.
(Included as a sheet in the Supplemental_tables.xls file.)

Table S5. Oligonucleotides used in the study.
(Included as a sheet in the Supplemental_tables.xls file.)